

Mechanical Stability of 2D Ti_2CO_x MXenes Under Compression Using Reactive Molecular Dynamics

Hossein Darban¹

Institute of Fundamental Technological Research, Polish Academy of Sciences, Pawińskiego 5B, 02-106 Warsaw, Poland

Abstract

The compressive and post-buckling behavior of Ti_2C and Ti_2CO_2 MXene nanosheets is studied using large-scale reactive molecular dynamics simulations. Nanosheets are subjected to uniaxial, biaxial, and shear loads to investigate their buckling modes, atomic-level deformation mechanisms, and failure characteristics. The results indicate that classical continuum mechanics significantly overestimates the buckling strains. Nanosheets exhibit higher resistance to buckling along the armchair direction than along the zigzag direction. Although atomic-scale defects reduce the buckling stress, they influence deformation only locally and do not alter the global buckling mode shapes. Lateral confinement pressure, such as that caused by polymerization-induced shrinkage in MXene–polymer composites, substantially increases the buckling stress. Oxygen surface termination increases the buckling stress from approximately 1 GPa to 3.5 GPa and reduces directional anisotropy in the elastic response. Under large compressive strains, Ti_2CO_2 nanosheets fracture, whereas Ti_2C nanosheets retain structural integrity at strains exceeding 0.35. Atomistic analysis reveals opposite stress states in the top and bottom Ti layers due to curvature-induced strain gradients. Under biaxial compression, the nanosheet buckles in a dome-like shape, whereas shear loads produce elliptical deflection modes. The presented findings stimulate future studies on MXene morphological transformations, such as the development of nanotube, nanoscroll, and folded architectures.

Keywords: MXene; In-plane stability; Surface termination; Mechanical analysis; Buckling; Molecular dynamics simulations.

1. Introduction

MXenes are a promising family of two-dimensional transition metal carbides, nitrides, or carbonitrides, discovered in 2011 [1]. The general formula for MXenes is $\text{M}_{n+1}\text{X}_n\text{T}_x$, where M is an early transition metal, X represents carbon or nitrogen, and T_x refers to surface terminations, including -OH, -O, or -F groups. MXenes have attracted widespread interest due to their remarkable optoelectronic and

¹- *Corresponding author: Hossein Darban; E-mail address: hdarban@ippt.pan.pl; Tel.: (+48) 22 826 12 81*

electrochemical characteristics, excellent electrical conductivity, hydrophilicity, and robust mechanical performance [2–8]. MXenes have been incorporated into several technologies, including energy storage and conversion systems, catalytic processes, water purification and desalination, electromagnetic interference shielding, communication devices, optical and electronic components, plasmonic systems, sensing and actuation platforms, structural composites, and biomedical applications [7,9–12]. In addition, MXenes can serve as high-performance reinforcements in composite materials for a broad range of applications. For instance, MXene–polymer composites have been explored for biomedical and anticorrosion applications [9,13,14].

The mechanical behavior of MXene nanosheets has been investigated through both experimental and computational approaches; however, experimental data remain limited due to the inherent difficulty of mechanically testing ultrathin 2D materials. Early nanoindentation measurements on single-layer $\text{Ti}_3\text{C}_2\text{T}_x$ MXene using atomic force microscopy reported an elastic modulus of 330 ± 30 GPa [15], notably higher than values obtained for graphene oxide and reduced graphene oxide under similar testing conditions [16,17]. More recently, advances in nanoscale sample fabrication and in-situ tensile testing have enabled direct uniaxial measurements of single-layer $\text{Ti}_3\text{C}_2\text{T}_x$ within an electron microscope, revealing an effective Young’s modulus of approximately 480 GPa, elastic strain limits of several percent, and tensile strengths exceeding 15 GPa [18].

First-principles simulations have provided further insight into MXene deformation mechanisms. Density functional theory (DFT) studies on Ti-based MXenes [19], including Ti_2C and Ti_3C_2 and their oxygen-functionalized forms, show that these 2D materials exhibit exceptional tensile flexibility. The DFT calculations predicted the detailed stress–strain behavior and revealed that the Ti_2CO_2 single-layer can withstand elastic strains exceeding 20%, surpassing even graphene under comparable loading conditions. Moreover, the predicted Young’s modulus of $\text{Ti}_3\text{C}_2\text{O}_2$ (≈ 500 GPa) aligns closely with the experimentally measured value reported in [18]. A recent review [20] further summarizes state-of-the-art DFT and machine-learning methodologies used to investigate MXene structure, properties, and behavior.

Investigating the mechanical properties of MXenes using molecular dynamics (MD) simulations is an active and insightful area of research. This progress has been largely driven by the development of advanced reactive force fields (ReaxFF) [21]. Because ReaxFF can dynamically model bond formation and bond breaking, it is particularly well-suited for capturing the complex deformation mechanisms that characterize these two-dimensional materials [22–29]. The current state of the art in the mechanical modeling of Ti_2CT_x and $\text{Ti}_3\text{C}_2\text{T}_x$ MXenes is primarily defined by two well-established ReaxFF parametrizations, originally introduced in [30,31]. A recent study assessed the performance of several

interatomic potentials in modeling the structural and elastic properties of titanium carbide and nitride MXenes [32]. The Charge-Optimized Many-Body (COMB3), ReaxFF, and Modified Embedded Atom Method (MEAM) potentials were evaluated by comparing their predictions of lattice parameters, layer thickness, and elastic constants against available DFT data. The results indicate that the ReaxFF parameterizations, in particular, offer some of the most reliable descriptions of titanium-based MXenes. The recent progress in ReaxFF force field developments for modeling the 2D materials is reviewed in [28].

Among the potentials discussed, the ReaxFF force field developed in [31] has been particularly effective for modeling MXenes. For example, it was used in [27] to demonstrate that oxygen functionalization strongly affects the tensile response of Ti_2C MXene, such as its stiffness, strength, and failure strain. Similarly, the work in [29] employed this potential to show that surface terminations significantly influence the elastic and fracture behavior of Ti-based MXenes. The potential has also been applied to study the friction and failure of $\text{Ti}_3\text{C}_2\text{T}_x$ under sliding [22], the reduction of fracture toughness due to atomic-scale defects in Ti_2C [23], and nanoindentation responses of Ti_2CO_2 and $\text{Ti}_3\text{C}_2\text{O}_2$, where point defects were found to lower the Young's modulus [24]. Additionally, the study in [25] used the same ReaxFF parameterization to demonstrate that surface termination engineering can effectively tailor the tensile properties of $\text{Ti}_3\text{C}_2\text{T}_x$ MXenes. Other classical MD potentials have also been employed to investigate the tensile and fracture behavior of various MXenes [6,26,33,34].

Most experimental and numerical studies on MXene nanosheets have focused on their tensile or flexural properties, while investigations of their compressive and shear behavior remain scarce. Understanding MXene deformation under compression and shear is, however, crucial for assessing their mechanical stability under realistic loading conditions. One notable exception is the work reported in [35], where in-situ uniaxial compression experiments on accordion-like multilayer Ti_2CT_x and $\text{Ti}_3\text{C}_2\text{T}_x$ revealed pronounced anisotropy and highly nonlinear deformation under both in-plane and out-of-plane loading. Through SEM-assisted nanoindentation, the study revealed progressive structural failure characterized by bending, buckling, tearing, shearing, kinking, and delamination as the compressive load increased.

In practical applications, such as flexible electronics or protective coatings, MXenes are often subjected to compressive or shear stresses. Moreover, during the fabrication of MXene-polymer composites, nanosheets can experience compressive loading due to polymerization-induced matrix shrinkage, a phenomenon also observed in carbon-nanotube-based composites [36]. Under such lateral confinement, MXene nanosheets may buckle, wrinkle, detach, or fail. Therefore, studying compressive and shear responses is essential for designing mechanically robust MXene-based materials and predicting

their performance under multifunctional operating conditions. However, such fundamental knowledge remains largely absent from the current literature. The present study aims to address this scientific gap by conducting a series of large-scale reactive molecular dynamics simulations using the well-established ReaxFF force field developed in [31].

2. Molecular Dynamics Simulations

Molecular dynamics (MD) simulations are employed in this work to investigate the mechanical response and stability of Ti_2C MXene under compression and shear. Both uniaxial and biaxial compression cases are considered. The effects of strain rate, lateral confinement pressure, vacancy defect, and O_2 surface termination on the response of Ti_2C MXene are studied.

The MD simulations are conducted using the Large Scale Atomic/Molecular Massively Parallel Simulator (LAMMPS) [37–39] and the ReaxFF force field developed in [31]. The obtained results are visualized using the Open Visualization Tool (OVITO) [40]. The simulations involve Ti_2C and Ti_2CO_2 MXene nanosheets with an in-plane dimension of $7 \times 7 \text{ nm}^2$, as shown in Fig. 1. The initial atomic configurations are constructed by replicating the unit cells obtained from [41] along in-plane directions in OVITO. Simulations are performed at 1 K to suppress local atomic thermal vibrations and isolate the intrinsic mechanical response of the 2D MXene nanosheets.

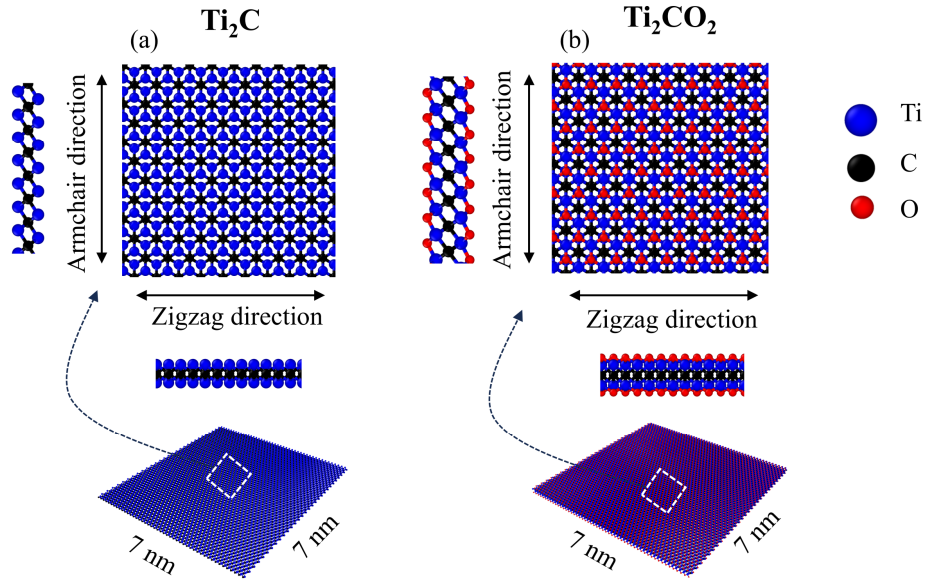


Fig. 1 Initial atomic configuration of (a) Ti_2C and (b) Ti_2CO_2 MXene nanosheets.

Three-dimensional simulations are run with non-periodic boundary conditions to model the behavior of a free-standing MXene nanosheet. After assigning the initial coordinates of atoms, the system undergoes an energy minimization process in which atomic positions are iteratively adjusted until both

the energy and force fall below predefined tolerances of 1×10^{-10} (dimensionless) and 1×10^{-10} (kcal/mol)/Å, respectively. This procedure relaxes the atomic configuration to a local energy minimum, thereby eliminating residual stresses. The minimization was conducted in LAMMPS using the conjugate gradient (CG) algorithm with the Polak–Ribiere (PR) formulation. This particular CG variant is recognized as highly efficient for diverse minimization tasks in atomistic modeling. The velocity form of the Stoermer-Verlet time integration algorithm (velocity-Verlet) is used [42].

Following minimization, atomic velocities at the studied temperature of 1 K are defined. Then, the system is equilibrated for 300 ps at the temperature of 1 K using the NVT ensemble, where the temperature is controlled using a Nose-Hoover thermostat. During equilibration, a lateral confinement pressure is applied to the MXene nanosheet to preserve its flat geometry and facilitate the onset of the first buckling mode (see Fig. 2 (d)). This effect is implemented by introducing repulsive walls positioned 1.6 Å above and below the MXene nanosheet, each interacting with the atoms within a cutoff distance of 1.5 Å. The interaction energy between a wall and an atom at a distance r follows the 9–3 Lennard-Jones potential, $E = \varepsilon \left(2/15 (\sigma/r)^9 - (\sigma/r)^3 \right)$ with $\varepsilon = 0.1$ kcal/mol and $\sigma = 1.74749$ Å. These parameter values are selected to maintain the flat geometry of the MXene nanosheet without exerting excessive repulsion. They also ensure that the force on the atoms is zero at the cutoff distance and increases progressively as atoms approach the wall.

The energy, temperature, and internal forces of the system are computed and monitored during equilibration to ensure the system is properly equilibrated before mechanical testing (see Fig. 2(a)-(c)). The confinement pressure is released at the end of the equilibration stage, before the application of deformation. This procedure may leave the nanosheet in a slightly pre-stressed state at the onset of loading. The deformation at an edge of the nanosheet is applied by displacing a few layers of atoms with a constant velocity corresponding to the desired strain rate. At each timestep, the strain is computed as the ratio of the applied displacement to the initial length of the nanosheet along the loading direction. The stress is obtained directly from LAMMPS output using the virial formulation. The effect of the simulation timestep is studied in Appendix A. To balance computational efficiency with numerical accuracy, a timestep of 0.2 fs is used for all simulations in this study, unless otherwise stated.

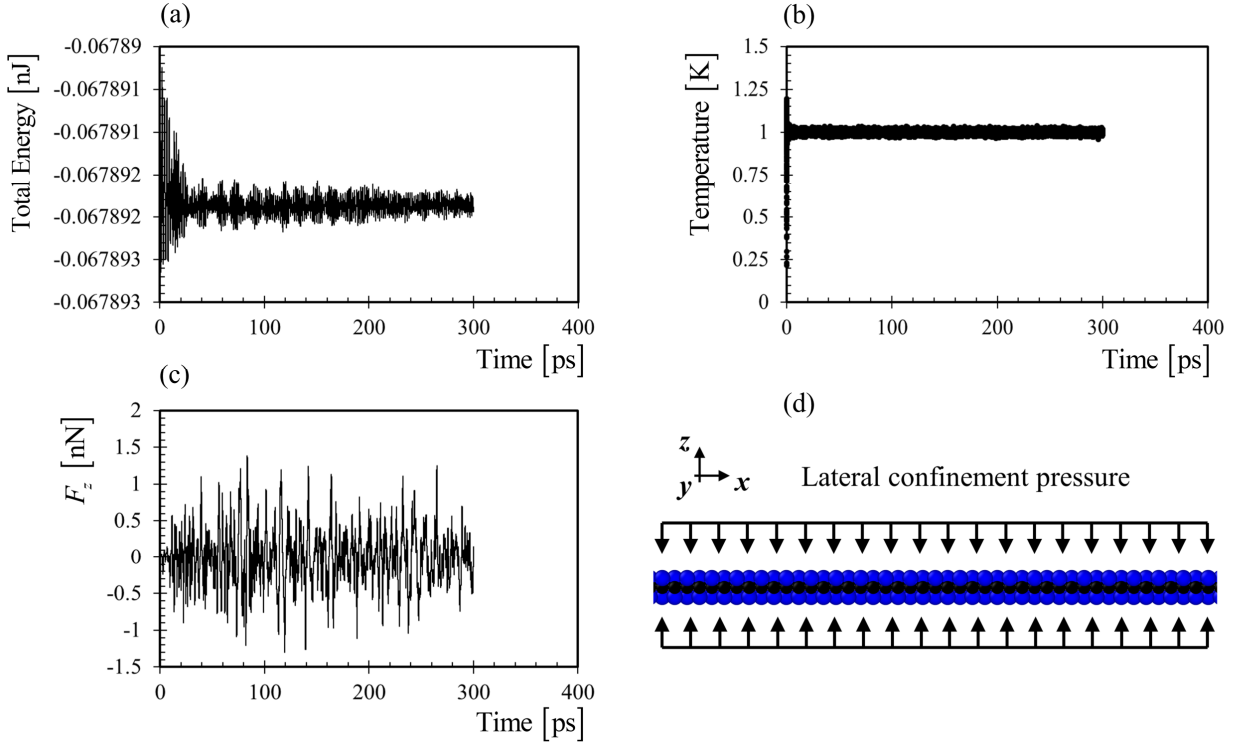


Fig. 2 Thermomechanical variables during equilibrium: (a) total energy, (b) temperature, and (c) out-of-plane force vs. time. (d) Schematic illustrating the lateral confinement pressure applied in the out-of-plane direction during equilibrium.

3. Results and Discussions

The computations in this study were carried out on the state-of-the-art supercomputer Ares, hosted by the Academic Computer Centre CYFRONET AGH in Kraków, Poland. One computing node, equipped with 48 cores provided by dual Intel Xeon Platinum 8268 processors (2.90 GHz) and 192 GB of RAM, was employed. The total wall-clock time for the simulations varied depending on the number of atoms in the model and the total simulation duration. For example, the simulations presented in Section 3.1, which investigate the strain rate effect, required approximately 40 hours to complete, whereas those described in Section 3.5 on post-buckling behavior took about one week.

3.1. Strain Rate Effect

The strain rate has a pronounced influence on the compressive response of nanosheets. This effect is demonstrated in Fig. 3 for a $7 \times 7 \text{ nm}^2$ Ti_2C MXene nanosheet. The stress–strain curves corresponding to compression along the armchair and zigzag directions are shown for four different strain rates. From the initial linear portion of the stress–strain curves, the Young’s moduli along the armchair and zigzag directions are determined to be 655 GPa and 590 GPa, respectively. These values are in good agreement with previously reported data from first-principles calculations for the tensile response of Ti_2C MXenes,

which indicate Young's moduli of approximately 600 GPa and 620 GPa along the armchair and zigzag directions, respectively [19].

MXene nanosheets subjected to higher compression rates exhibit buckling at higher stress and strain levels and display more unstable post-buckling behavior, characterized by stress oscillations of greater amplitude. As the strain rate decreases, the buckling stress tends to converge, and for the two lowest strain rates, the buckling stress values become nearly identical. The curves in Fig. 3(c) compare the compressive response of the MXene nanosheet along the armchair and zigzag directions at the lowest strain rate. As shown, the nanosheet sustains higher stresses when compressed along the armchair direction. For compression along the armchair direction, the Ti_2C MXene nanosheet exhibits buckling at a stress and strain of approximately 1 GPa and 0.0015, whereas buckling occurs at about 0.6 GPa and 0.0006 when compressed along the zigzag direction. The predicted buckling strain of 0.0006 for the zigzag-oriented loading case is affected by residual stresses present at zero strain.

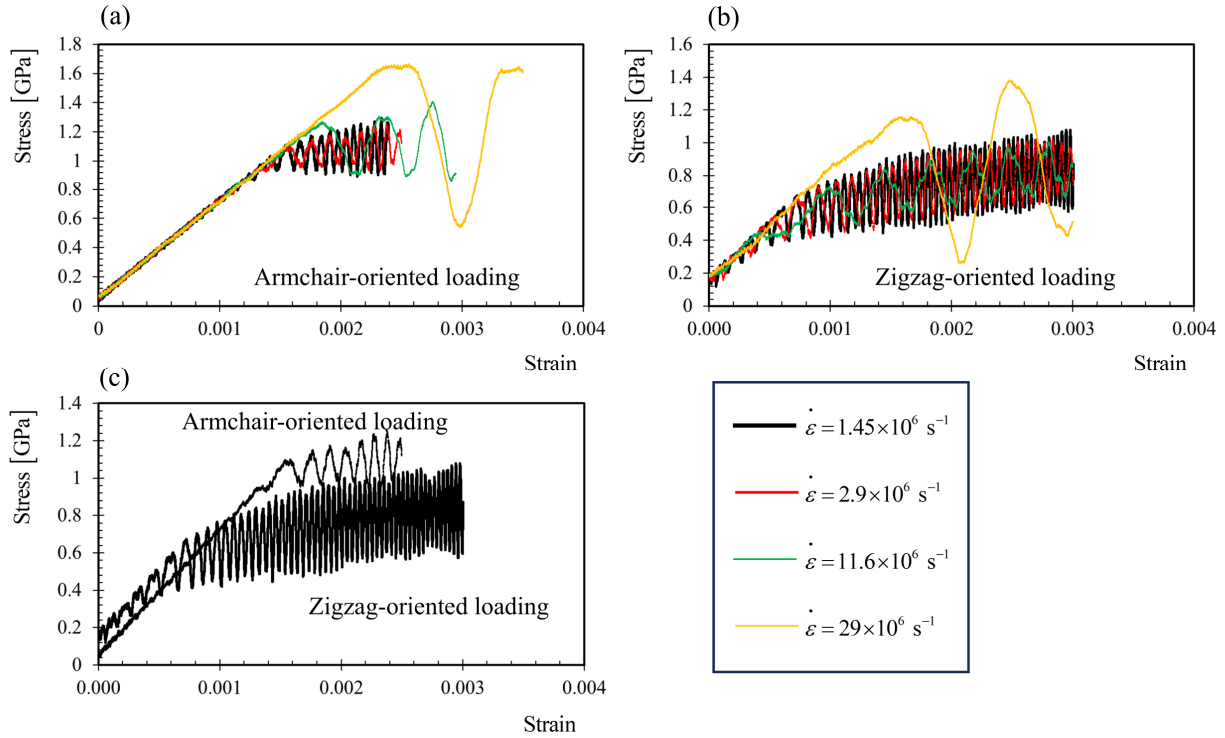


Fig. 3 Stress-strain curves of Ti_2C MXene nanosheets with an in-plane dimension of $7 \times 7 \text{ nm}^2$ under compression along (a) the armchair direction and (b) the zigzag direction at different strain rates. (c) Comparison of the stress-strain curves under armchair- and zigzag-oriented loading at a strain rate of $1.45 \times 10^6 \text{ s}^{-1}$ and timestep of 0.2 fs.

The adopted simulation setup induces the plate-like first buckling mode in Ti_2C MXene nanosheets. The corresponding buckling mode shapes at different applied strains are shown in Fig. 4 for loadings along both the armchair and zigzag directions. At a strain of 0.00117, the nanosheet already exhibits

buckling under zigzag compression, while it remains flat under loading along the armchair direction. With increasing strain, the maximum out-of-plane deflection, occurring at the midsection of the nanosheet, grows progressively, with the deflection under armchair-oriented loading consistently smaller than that under zigzag-oriented loading. In both loading directions, the buckling mode shapes display the inherent symmetry associated with mode I deformation.

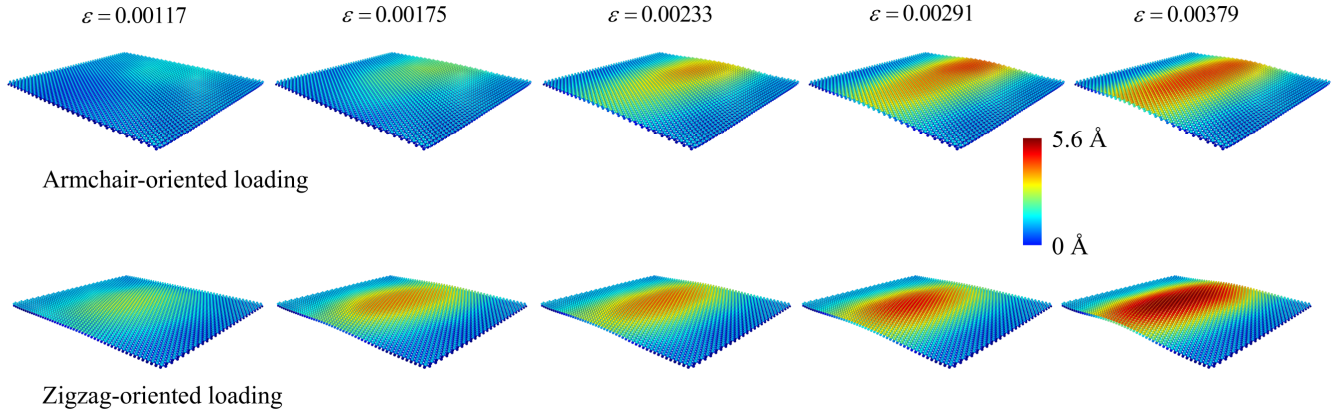


Fig. 4 Buckling mode shapes of Ti_2C MXene nanosheets with an in-plane dimension of $7 \times 7 \text{ nm}^2$ under progressive compression along the armchair and the zigzag directions at the strain rate of $2.9 \times 10^6 \text{ s}^{-1}$ and timestep of 0.2 fs. Color maps represent the out-of-plane deflections.

A three-dimensional finite element model (FEM) of an isotropic plate with dimensions $7 \times 7 \times 0.231 \text{ nm}^2$, clamped along the loaded edges and free along the unloaded ones, analogous to the Ti_2C MXene nanosheets studied, yielded a buckling strain of 0.0036. Comparison of the FEM-predicted buckling strain (0.0036) with that obtained from MD simulations (0.0015 for the armchair-oriented loading) demonstrates that the classical continuum mechanics framework overpredicts the critical strain and is inadequate for describing the buckling behavior of Ti_2C MXene nanosheets.

3.2. Effect of Vacancy Defect

MXene nanosheets may contain vacancy defects, either inherited from their MAX phase precursors or generated during the chemical etching process. The presence of such defects reduces the stiffness of MXenes, making them more susceptible to mechanical instabilities under compression. In this section, the effect of vacancy defects on the compressive response of Ti_2C MXene nanosheets is investigated. Fig. 5 presents the stress–strain curves and associated buckling configurations for nanosheets with in-plane dimensions of $7 \times 7 \text{ nm}^2$, compressed along the armchair and zigzag directions with varying vacancy concentrations. The simulations were conducted at a strain rate of $2.9 \times 10^6 \text{ s}^{-1}$, using a timestep of 0.2 fs.

The desired vacancy concentration is introduced by randomly removing the corresponding number of atoms from the simulation box.

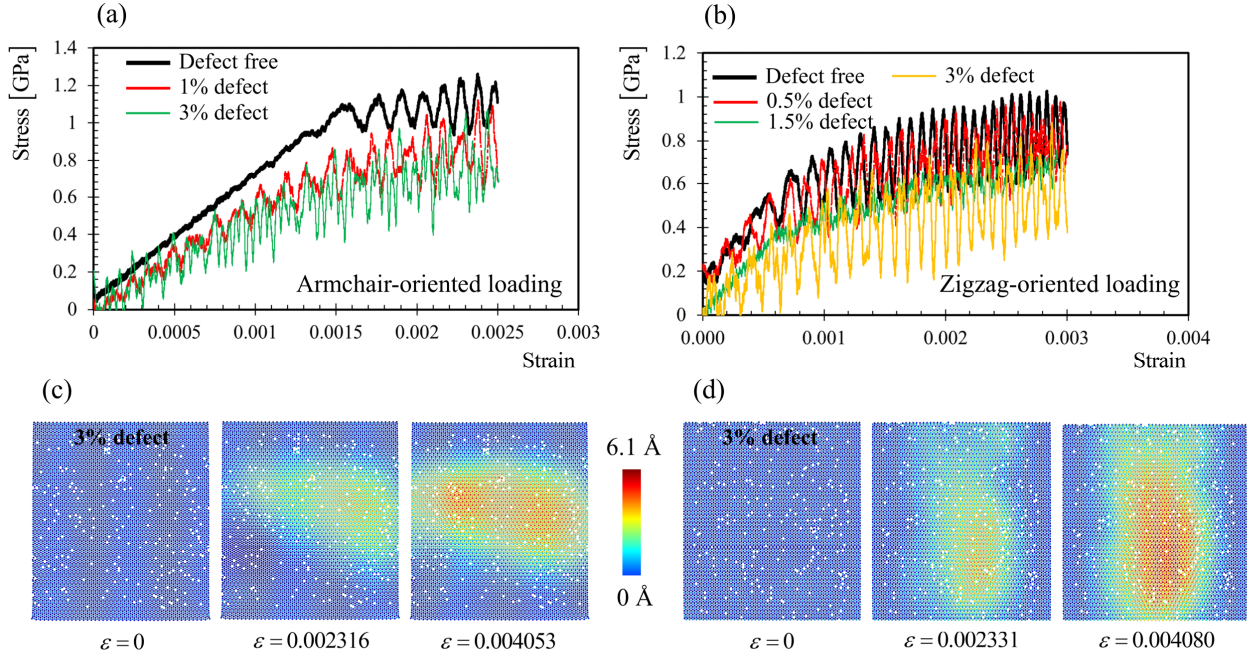


Fig. 5 Stress-strain curves of Ti_2C MXene nanosheets with an in-plane dimension of $7 \times 7 \text{ nm}^2$ under compression along (a) the armchair direction and (b) the zigzag direction for different percentages of vacancy defects at the strain rate of $2.9 \times 10^6 \text{ s}^{-1}$ and timestep of 0.2 fs. Buckling mode shapes related to compression along (c) the armchair and (d) the zigzag directions. Color maps represent the out-of-plane deflections.

The stress–strain curves in Fig. 5(a) and (b) reveal a clear dependence of the compressive response of Ti_2C MXene nanosheets on the concentration of vacancy defects. As the defect percentage increases, a noticeable reduction in peak stress is observed for both loading directions, reflecting the degradation of stiffness and structural integrity. In addition to lowering the critical buckling stress, vacancy defects also alter the post-buckling behavior. Higher defect concentrations lead to increased amplitude of stress oscillations in the post-buckling regime, indicating reduced stability and greater susceptibility to local structural collapse. This observation is further supported by the buckling configurations shown in Fig. 5(c) and (d), where larger out-of-plane deflections are evident in regions with a higher concentration of vacancy defects. The vacancy defect exhibits no significant influence on the buckling strain.

3.3. Lateral Confinement Pressure Effect

In this section, we examine how confinement pressure influences the compressive response of Ti_2C MXene nanosheets. The lateral confinement pressure during the deformation stage is introduced by positioning two layers of harmonic springs above and below the MXene nanosheet with an initial gap of 0.1 Å. Simulations are then performed for various spring stiffness values, and the corresponding stress–strain responses are shown in Fig. 6. These results refer to Ti_2C MXene nanosheets with an in-plane dimension of $7 \times 7 \text{ nm}^2$ subjected to compression along the armchair direction at a strain rate of $11.6 \times 10^6 \text{ s}^{-1}$ using a timestep of 0.2 fs. As shown by the stress–strain curves, applying a lateral confinement pressure increases the buckling stress and strain, reduces the amplitude of post-buckling stress oscillations, and has no effect on the slope of the curves. For example, a Ti_2C MXene embedded in a medium with a stiffness of 0.001 (kcal/mol)/Å 2 exhibits nearly twice the buckling stress and strain of a free-standing MXene.

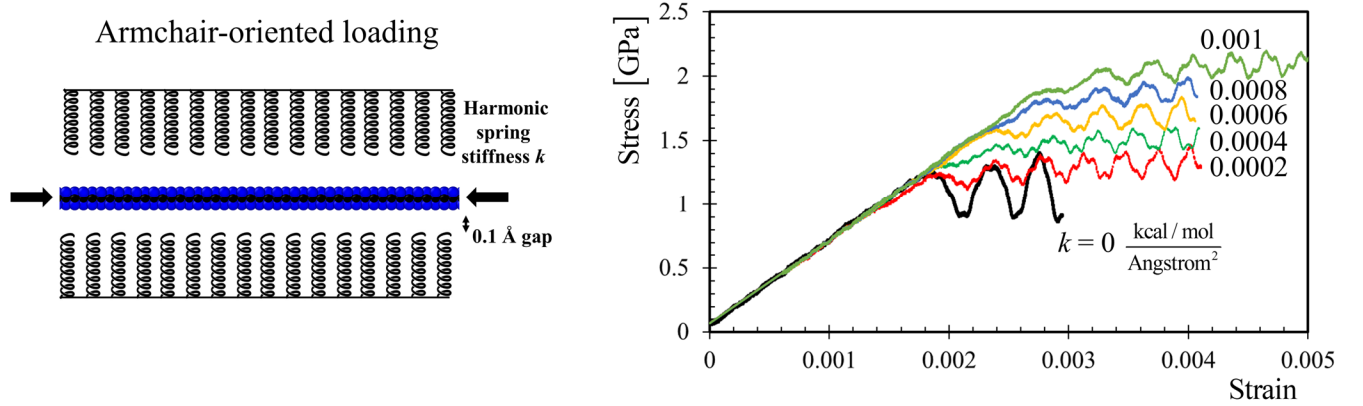


Fig. 6 Stress-strain curves of Ti_2C MXene nanosheets with an in-plane dimension of $7 \times 7 \text{ nm}^2$ under compression along the armchair direction for different lateral confinement pressures at the strain rate of $11.6 \times 10^6 \text{ s}^{-1}$ and timestep of 0.2 fs.

3.4. Effect of O_2 Surface Termination

MXenes typically exhibit surface terminations such as $-\text{O}$, $-\text{OH}$, or $-\text{F}$ as a result of their synthesis routes, providing opportunities to tailor their properties. In this section, we examine how $-\text{O}$ termination influences the compressive behavior of Ti_2C MXene nanosheets. For this purpose, Ti_2C and Ti_2CO_2 nanosheets with in-plane dimensions of $7 \times 7 \text{ nm}^2$ are simulated under compression along both the armchair and zigzag directions at a strain rate of $11.6 \times 10^6 \text{ s}^{-1}$ using a timestep of 0.2 fs. The obtained stress-strain curves are illustrated in Fig. 7.

The $-\text{O}$ surface termination leads to a substantial increase in the buckling stress of the MXene nanosheets. For the geometry considered here, the buckling stress rises from roughly 1 GPa to nearly 3.5

GPa. This enhancement is primarily attributed to the increased effective thickness introduced by the termination groups, which in turn raises the second moment of area and thus the bending stiffness of the nanosheet. Another notable outcome is that $-O$ termination reduces the anisotropy between the responses under armchair and zigzag loading. Furthermore, the Young's moduli of Ti_2C nanosheets, 655 GPa along the armchair direction and 590 GPa along the zigzag direction, decrease to approximately 480 GPa in Ti_2CO_2 . This reduction aligns with first-principles predictions reported in [19]. However, the Young's modulus values for Ti_2CO_2 provided in [19] are higher, reported as 540 GPa (armchair) and 593 GPa (zigzag).

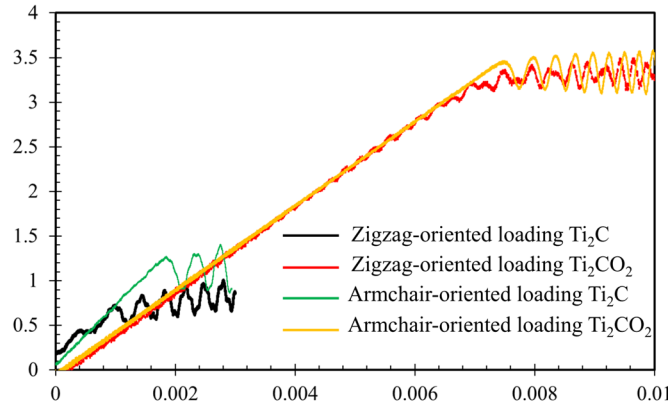


Fig. 7 Stress-strain curves of Ti_2C and Ti_2CO_2 MXene nanosheets with an in-plane dimension of $7 \times 7 \text{ nm}^2$ under compression along the armchair and the zigzag directions at the strain rate of $11.6 \times 10^6 \text{ s}^{-1}$ and timestep of 0.2 fs.

3.5. Post-Buckling

To examine the post-buckling behavior of Ti_2C nanosheets, additional simulations are performed at a higher strain rate of $58 \times 10^6 \text{ s}^{-1}$ to maintain a feasible computational cost. Both defect-free and 2% defective Ti_2C MXene nanosheets with an in-plane dimension of $7 \times 7 \text{ nm}^2$ are subjected to progressive compression along the armchair direction. The resulting buckling mode shapes are presented in Fig. 8. The simulations are extended to strains exceeding 0.26, during which no fracture is observed. The presence of defects does not noticeably alter the global buckling patterns, even at these large strains, indicating that their influence remains localized.

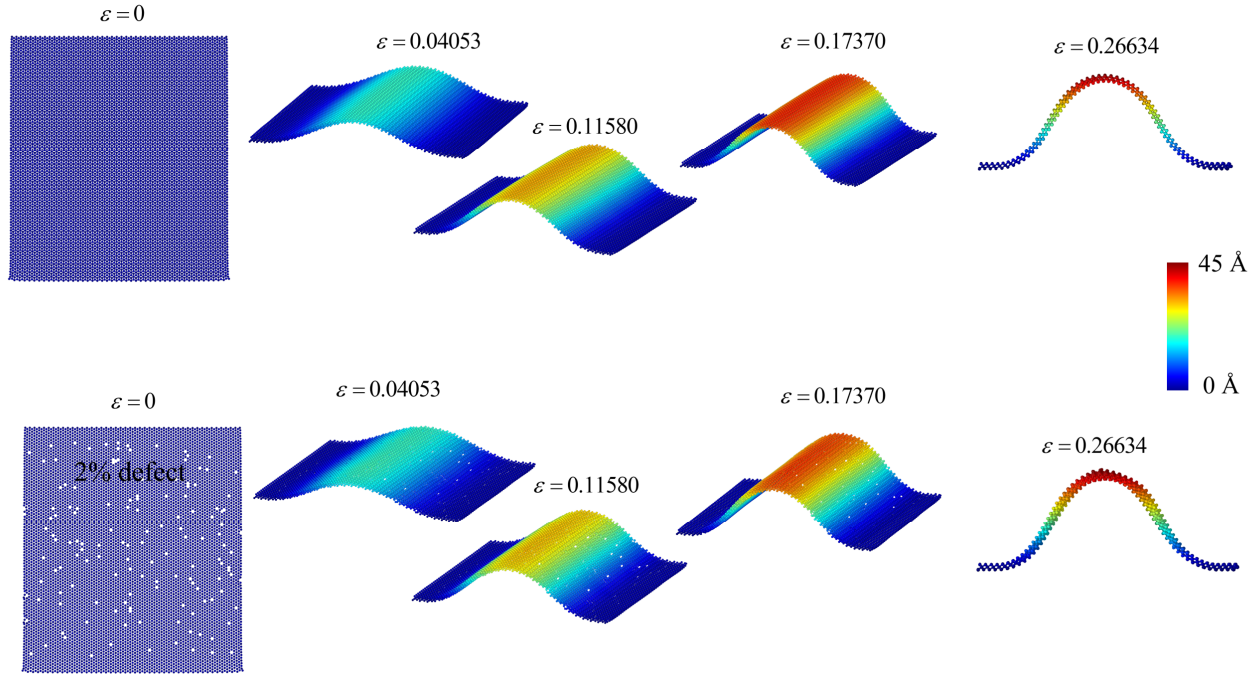


Fig. 8 Buckling mode shapes of defect-free and 2% defective Ti_2C MXene nanosheets with an in-plane dimension of $7 \times 7 \text{ nm}^2$ under progressive compression along the armchair direction at the strain rate of $58 \times 10^6 \text{ s}^{-1}$ and timestep of 0.2 fs. Color maps represent the out-of-plane deflections.

Although the Ti_2C MXene nanosheets do not fracture under buckling, even at high strain levels, their lattice structure undergoes notable adjustments to accommodate the strain distribution through the thickness. For example, in the central region of the nanosheet shown in Fig. 8, the curvature bends downward. This implies that the upper Ti layer experiences tensile strain along the loading direction, whereas the lower Ti layer is subjected to compression. This behavior is illustrated in Fig. 9, which displays the evolution of Ti–Ti and C–C bond lengths during loading; bonds longer than 3.08 Å are omitted for clarity.

As shown, the upper Ti layer develops bond lengths exceeding 3.08 Å along the loading direction in the central region, while the bond lengths perpendicular to the load remain mostly unchanged. In contrast, the lower Ti layer shows shortened bonds in the same central region. Moving toward the first and last quarters of the nanosheet, the trend reverses: the lower Ti layer exhibits increased bond lengths along the loading direction, whereas the upper layer's bond lengths decrease. The C–C bonds remain largely unaffected throughout the deformation process, though at high strain levels, a slight elongation along the loading direction can be observed at the left, center, and right sections of the nanosheet.

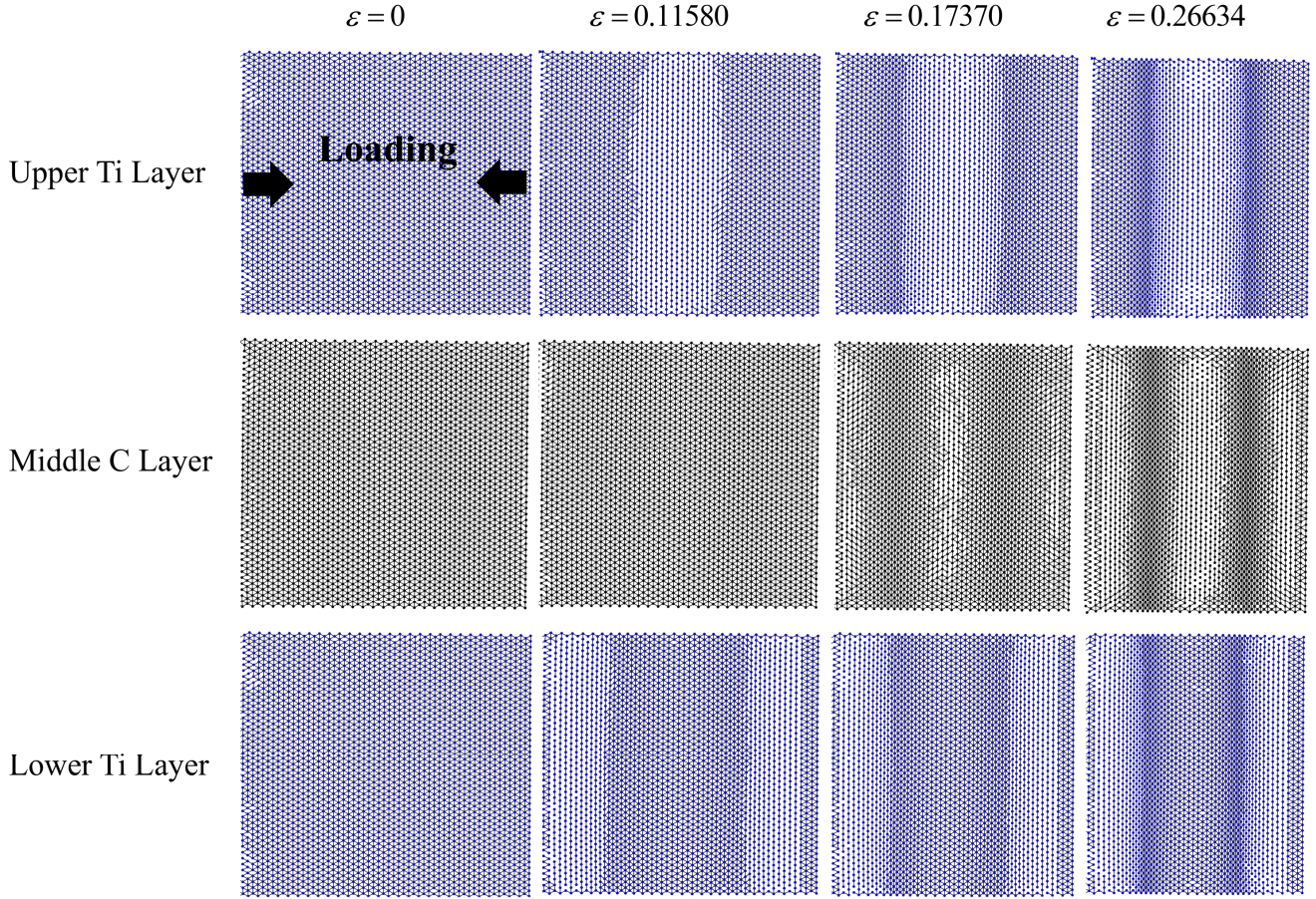


Fig. 9 Analysis of Ti-Ti and C-C bond lengths in a Ti_2C MXene nanosheet with an in-plane dimension of $7 \times 7 \text{ nm}^2$ under progressive compression along the armchair direction at the strain rate of $58 \times 10^6 \text{ s}^{-1}$ and timestep of 0.2 fs. Bonds with lengths higher than 3.08 \AA are not shown.

To examine how the lattice structure evolves under loading, the variations in Ti–Ti and C–C bond lengths and bond angles are tracked within a small representative cell located at the center of the nanosheet. This cell consists of three atoms in each of the Ti–C–Ti layers. As illustrated in Fig. 10, the three atoms in each layer form an equilateral triangle.

For the upper Ti layer, the bond lengths are labeled U_1 , U_2 , and U_3 , with the corresponding angles denoted as θ_{12} , θ_{13} , and θ_{23} . U_1 represents the bond length perpendicular to the loading direction and remains nearly constant throughout deformation. In contrast, U_2 and U_3 increase almost equally as the applied strain grows, confirming that the upper Ti layer experiences tensile deformation in the central region of the nanosheet. For instance, at the strain of 0.25, the bond length U_2 is stretched by 0.16 \AA . Consistent with the changes in the bond lengths, θ_{12} and θ_{13} increase, whereas θ_{23} decreases. In the lower Ti layer, L_1 , the bond length perpendicular to the loading direction also remains mostly unchanged. However, L_2 and L_3 decrease with increasing strain, indicating compression of the lower-layer Ti atoms. The

corresponding bond angles adjust in a manner consistent with this compressive deformation. The C–C bonds and angles in the middle carbon layer exhibit only minor changes during loading, reflecting the relatively lower sensitivity of this layer to the imposed deformation.

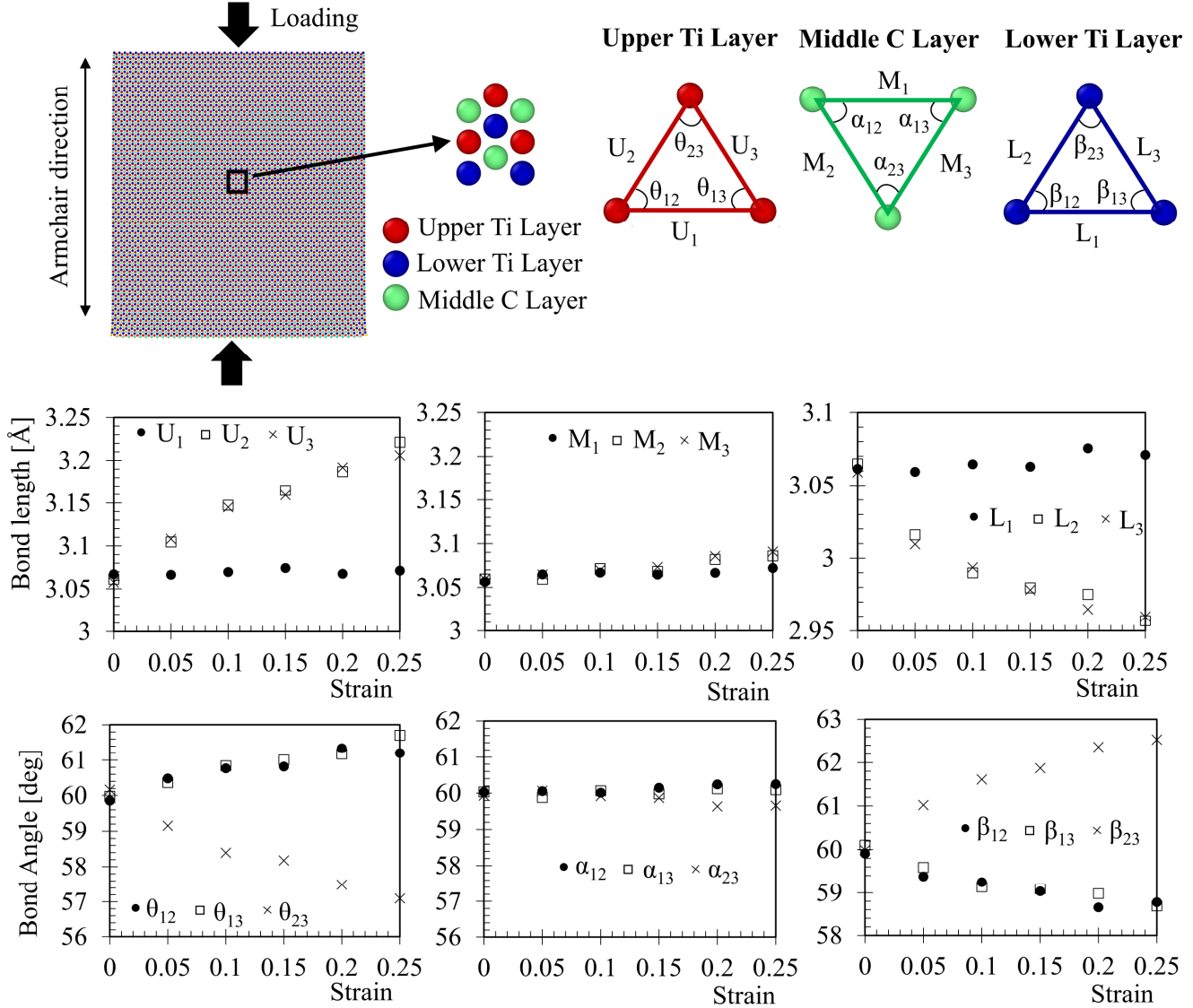


Fig. 10 Variations of Ti-Ti and C-C bond lengths and angles in the center of Ti_2C MXene nanosheet with an in-plane dimension of $7 \times 7 \text{ nm}^2$ under progressive compression along the armchair direction at the strain rate of $58 \times 10^6 \text{ s}^{-1}$ and timestep of 0.2 fs.

To assess how $-\text{O}$ surface termination influences the post-buckling behavior, we performed additional simulations on Ti_2C and Ti_2CO_2 MXene nanosheets with in-plane dimensions of $7 \times 7 \text{ nm}^2$. The nanosheets were compressed along both the armchair and zigzag directions at an elevated strain rate of $5.7 \times 10^8 \text{ s}^{-1}$ using a timestep of 1 fs. These higher values were chosen to keep the computational cost

manageable. The corresponding stress–strain responses are presented in Fig. 11. The Ti_2C nanosheets exhibit a smooth bending deformation without any signs of fracture, even at strains as large as 0.35. In contrast, the Ti_2CO_2 nanosheets fractured completely in the middle section. The fracture strain is notably higher when the Ti_2CO_2 nanosheet is loaded along the zigzag direction compared to loading along the armchair direction.

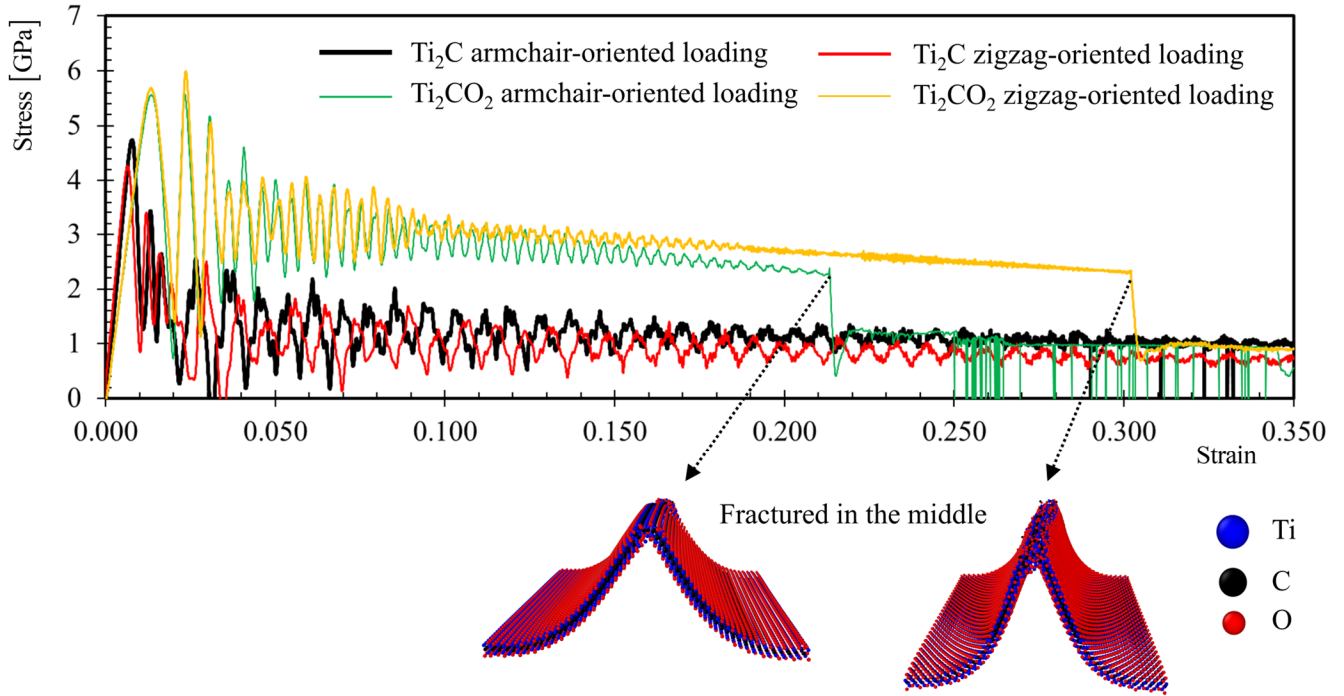


Fig. 11 Stress-strain curves of Ti_2C and Ti_2CO_2 MXene nanosheets with an in-plane dimension of $7 \times 7 \text{ nm}^2$ under compression along the armchair and the zigzag directions at the strain rate of $5.7 \times 10^8 \text{ s}^{-1}$ and timestep of 1 fs.

3.6. Biaxial and Shear Buckling

The buckling behavior of a Ti_2C MXene nanosheet with in-plane dimensions of $7 \times 7 \text{ nm}^2$ under biaxial compression is examined in this section. The nanosheet is compressed uniformly along both in-plane directions at a strain rate of $2.9 \times 10^6 \text{ s}^{-1}$. The resulting buckling mode shapes, shown in Fig. 12(a), display maximum out-of-plane deflection at the nanosheet's center. The iso-deformation contours (lines connecting atoms with equal deflection) form nearly concentric circles, indicating a symmetric buckling pattern. The corresponding stress–strain curves are provided in Fig. 12(b). The stress–strain curves along the armchair and zigzag directions nearly coincide, consistent with the symmetric deformation mode. The resulting dome-like buckling pattern further reflects the similarity in in-plane stiffness of the two directions and the uniformity of the applied load.

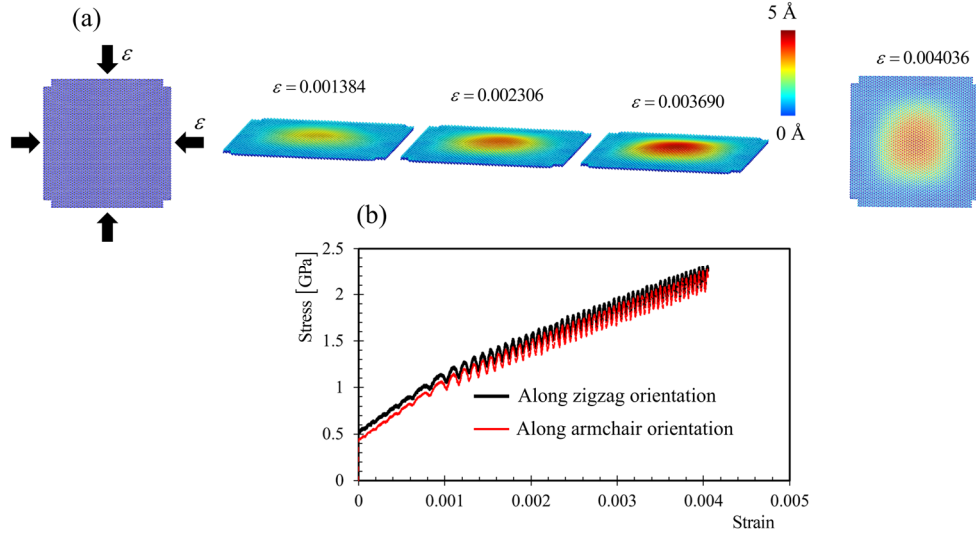


Fig. 12 (a) Buckling mode shapes of a Ti_2C MXene nanosheet with an in-plane dimension of $7 \times 7 \text{ nm}^2$ under a biaxial compression with the strain rate of $2.9 \times 10^6 \text{ s}^{-1}$ and timestep of 0.2 fs. Color maps represent the out-of-plane deflections. (b) Stress-strain curves along the armchair and the zigzag directions.

The response of the same Ti_2C MXene nanosheet under pure shear deformation is presented in Fig. 13. Shear is applied by displacing the atoms in the manner illustrated in the figure, using a velocity of $5 \times 10^{-7} \text{ Å/fs}$. Under this loading, the iso-deformation contours form nearly concentric ellipses aligned with the shear direction. As the imposed shear increases, the nanosheet exhibits progressively larger out-of-plane deflection.

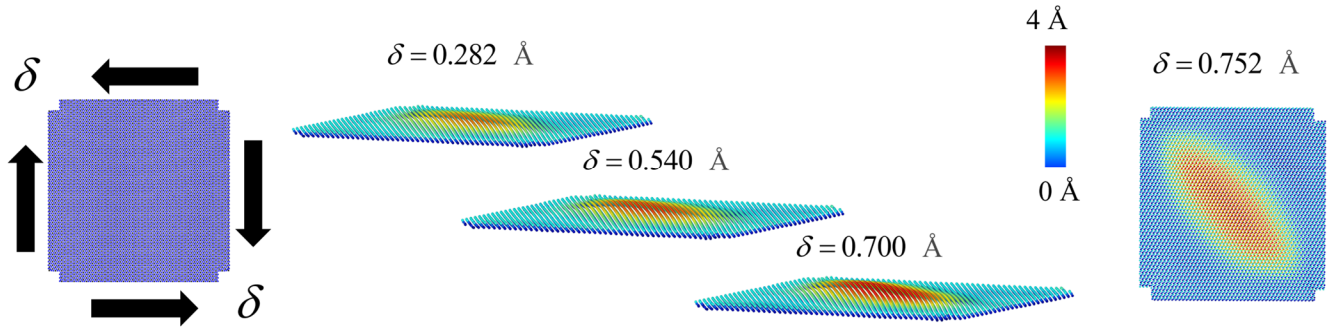


Fig. 13 Buckling mode shapes of a Ti_2C MXene nanosheet with an in-plane dimension of $7 \times 7 \text{ nm}^2$ under a shear loading. The displacement δ is applied with a velocity of $5 \times 10^{-7} \text{ Å/fs}$, and the timestep is 0.2 fs. Color maps represent the out-of-plane deflections.

4. Conclusions

A comprehensive atomistic investigation into the compressive and post-buckling behavior of Ti_2C and Ti_2CO_2 MXene nanosheets has been presented in this study using large-scale reactive molecular

dynamics simulations. The results demonstrate that classical continuum mechanics significantly overestimates the buckling strains of two-dimensional MXenes, underscoring the need for atomistic simulations or nonclassical continuum theories for accurate stability predictions. Ti_2C nanosheets exhibit greater resistance to buckling along the armchair direction than along the zigzag direction. Higher strain rates shift the onset of buckling to higher stress and strain levels and induce a more unstable post-buckling response characterized by larger stress oscillations. Although atomic-scale defects reduce buckling loads, they do not modify the global deformation mode. Surface termination has a pronounced effect on compressive stability: oxygen termination substantially increases the buckling stress and strain, and reduces directional anisotropy in the elastic response. At large compressive strains, Ti_2CO_2 nanosheets undergo fracture, whereas Ti_2C nanosheets retain structural integrity even beyond strains of 0.35. The simulations further show that lateral confinement pressure strongly enhances buckling resistance and mitigates post-buckling oscillations. Under biaxial compression, the nanosheets buckle into a dome-like shape, while shear loading yields elliptical deflection modes.

The findings in this paper highlight the complex interplay among surface chemistry, defect structure, and loading conditions in governing the mechanical stability of MXene nanosheets. These insights provide both fundamental understanding and practical guidance for the design and optimization of MXene-based composites, flexible electronics, and nanoscale structural components where compressive stability is essential. Additionally, the present results can stimulate future explorations of MXene morphological transformations, including the emergence of nanotube, nanoscroll, and folded architectures.

Declaration of interests

The author declares that he has no known competing financial interests or personal relationships that could have appeared to influence the work reported in this paper.

Funding

This research did not receive any specific grant from funding agencies in the public, commercial, or not-for-profit sectors.

Acknowledgements

The author gratefully acknowledges Polish high-performance computing infrastructure PLGrid (HPC Centers: WCSS, ACK Cyfronet AGH) for providing computer facilities and support within computational grant no. PLG/2025/018166.

Appendix A: Timestep Effect

The timestep of the MD simulations affects the results, particularly at higher strain rates. This is illustrated in Fig. A1, where stress-strain curves are presented for Ti_2C MXene nanosheets with an in-plane dimension of $7 \times 7 \text{ nm}^2$ under compression along the armchair direction at various strain rates and timesteps. The total wall-clock time required for the simulations increases as the timestep decreases. To balance computational efficiency with numerical accuracy, a timestep of 0.2 fs is used for all simulations in this study, unless otherwise stated.

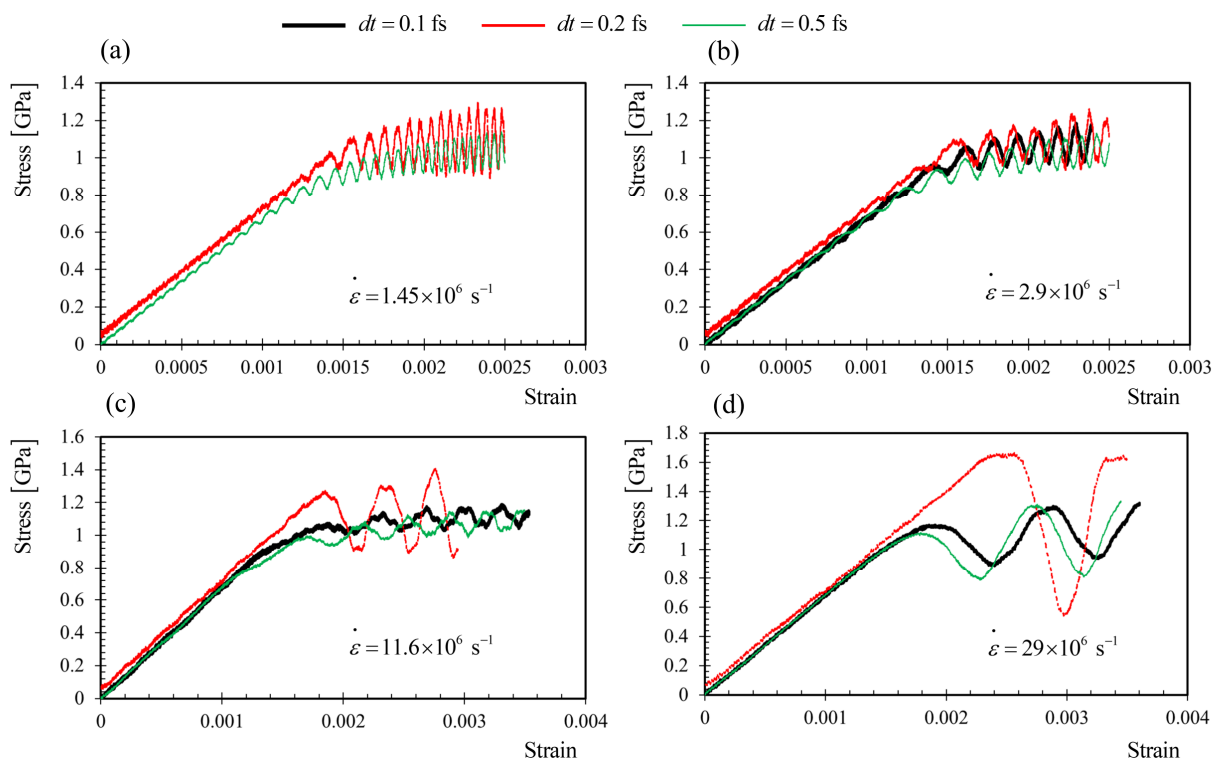


Fig. A1 (a)-(d) Stress-strain curves of Ti_2C MXene nanosheets with an in-plane dimension of $7 \times 7 \text{ nm}^2$ under compression along the armchair direction at different strain rates and timesteps.

References

- [1] M. Naguib, M. Kurtoglu, V. Presser, J. Lu, J. Niu, M. Heon, L. Hultman, Y. Gogotsi, M.W. Barsoum, Two-Dimensional Nanocrystals Produced by Exfoliation of Ti_3AlC_2 , *Advanced Materials* 23 (2011) 4248–4253. <https://doi.org/10.1002/adma.201102306>.
- [2] G. Murali, J.K. Reddy Modigunta, Y.H. Park, J.-H. Lee, J. Rawal, S.-Y. Lee, I. In, S.-J. Park, A Review on MXene Synthesis, Stability, and Photocatalytic Applications, *ACS Nano* 16 (2022) 13370–13429. <https://doi.org/10.1021/acsnano.2c04750>.
- [3] G. Murali, J. Rawal, J.K.R. Modigunta, Y.H. Park, J.-H. Lee, S.-Y. Lee, S.-J. Park, I. In, A review on MXenes: new-generation 2D materials for supercapacitors, *Sustainable Energy Fuels* 5 (2021) 5672–5693. <https://doi.org/10.1039/D1SE00918D>.

- [4] Y. Zhang, Z. Zhou, J. Lan, P. Zhang, Prediction of $\text{Ti}_3\text{C}_2\text{O}_2$ MXene as an effective capturer of formaldehyde, *Applied Surface Science* 469 (2019) 770–774. <https://doi.org/10.1016/j.apsusc.2018.11.018>.
- [5] Z. Shi, S. Zhong, Z. Zhang, Y. Sui, J. Zhou, L. Wu, Atomic insights into monolayer MXene degradation and impacts for lithium-ion storage, *Applied Surface Science* 689 (2025) 162506. <https://doi.org/10.1016/j.apsusc.2025.162506>.
- [6] S.M. Hatam-Lee, A. Esfandiar, A. Rajabpour, Mechanical behaviors of titanium nitride and carbide MXenes: A molecular dynamics study, *Applied Surface Science* 566 (2021) 150633. <https://doi.org/10.1016/j.apsusc.2021.150633>.
- [7] A. VahidMohammadi, J. Rosen, Y. Gogotsi, The world of two-dimensional carbides and nitrides (MXenes), *Science* 372 (2021) eabf1581. <https://doi.org/10.1126/science.abf1581>.
- [8] X. Xu, T. Guo, M. Lanza, H.N. Alshareef, Status and prospects of MXene-based nanoelectronic devices, *Matter* 6 (2023) 800–837. <https://doi.org/10.1016/j.matt.2023.01.019>.
- [9] H. Cao, Beyond graphene and boron nitride: why MXene can be used in composite for corrosion protection on metals?, *Composites Part B: Engineering* 271 (2024) 111168. <https://doi.org/10.1016/j.compositesb.2023.111168>.
- [10] T.T. Huynh, H.Q. Pham, Defect and non-metallic doping co-engineering in two-dimensional transition-metal carbide-based electrocatalysts for renewable energy conversion, *Coordination Chemistry Reviews* 549 (2026) 217254. <https://doi.org/10.1016/j.ccr.2025.217254>.
- [11] Y. Liu, D. Lv, Y. Yang, L. Zhu, R. Wang, S. Chen, D. Jiang, H. Wang, Multi-dimensional applications of MXene in human health: From disease prevention, diagnosis, to rehabilitation, *Journal of Materials Science & Technology* 246 (2026) 187–219. <https://doi.org/10.1016/j.jmst.2025.02.086>.
- [12] Y. Yao, X. Li, K.M. Sisican, R.M.C. Ramos, M. Judicpa, S. Qin, J. Zhang, J. Yao, J.M. Razal, K.A.S. Usman, Progress towards efficient MXene sensors, *Commun Mater* 6 (2025) 210. <https://doi.org/10.1038/s43246-025-00907-y>.
- [13] I. Amin, H. van den Brekel, K. Nemani, E. Batyrev, A. de Vooy, H. van der Weijde, B. Anasori, N.R. Shiju, $\text{Ti}_3\text{C}_2\text{T}_x$ MXene Polymer Composites for Anticorrosion: An Overview and Perspective, *ACS Appl. Mater. Interfaces* 14 (2022) 43749–43758. <https://doi.org/10.1021/acsami.2c11953>.
- [14] L. Kabir, K. Wijaya, S. Sagadevan, J. Unruangsri, K. Ullah, W.-C. Oh, 2D MXene-polymer based composites for biomedical applications, *Journal of Alloys and Compounds* 1031 (2025) 181068. <https://doi.org/10.1016/j.jallcom.2025.181068>.
- [15] A. Lipatov, H. Lu, M. Alhabeab, B. Anasori, A. Gruverman, Y. Gogotsi, A. Sinitskii, Elastic properties of 2D $\text{Ti}_3\text{C}_2\text{T}_x$ MXene monolayers and bilayers, *Science Advances* 4 (2018) eaat0491. <https://doi.org/10.1126/sciadv.aat0491>.
- [16] J.W. Suk, R.D. Piner, J. An, R.S. Ruoff, Mechanical Properties of Monolayer Graphene Oxide, *ACS Nano* 4 (2010) 6557–6564. <https://doi.org/10.1021/nn101781v>.
- [17] C. Gómez-Navarro, M. Burghard, K. Kern, Elastic Properties of Chemically Derived Single Graphene Sheets, *Nano Lett.* 8 (2008) 2045–2049. <https://doi.org/10.1021/nl801384y>.
- [18] C. Rong, T. Su, Z. Li, T. Chu, M. Zhu, Y. Yan, B. Zhang, F.-Z. Xuan, Elastic properties and tensile strength of 2D $\text{Ti}_3\text{C}_2\text{T}_x$ MXene monolayers, *Nat Commun* 15 (2024) 1566. <https://doi.org/10.1038/s41467-024-45657-6>.

- [19] Z. Guo, J. Zhou, C. Si, Z. Sun, Flexible two-dimensional $Ti_{n+1}C_n$ ($n = 1, 2$ and 3) and their functionalized MXenes predicted by density functional theories, *Phys. Chem. Chem. Phys.* 17 (2015) 15348–15354. <https://doi.org/10.1039/C5CP00775E>.
- [20] J.D. Gouveia, T.L.P. Galvão, K. Iben Nassar, J.R.B. Gomes, First-principles and machine-learning approaches for interpreting and predicting the properties of MXenes, *Npj 2D Mater Appl* 9 (2025) 8. <https://doi.org/10.1038/s41699-025-00529-5>.
- [21] K. Chenoweth, A.C.T. van Duin, W.A. Goddard, ReaxFF Reactive Force Field for Molecular Dynamics Simulations of Hydrocarbon Oxidation, *J. Phys. Chem. A* 112 (2008) 1040–1053. <https://doi.org/10.1021/jp709896w>.
- [22] Q. Yang, S.J. Eder, A. Martini, P.G. Grützmacher, Effect of surface termination on the balance between friction and failure of $Ti_3C_2T_x$ MXenes, *Npj Mater Degrad* 7 (2023) 6. <https://doi.org/10.1038/s41529-023-00326-9>.
- [23] I. Greenfeld, S. Jiang, L. Yang, H.D. Wagner, Nonlinear elasticity degrades monolayer fracture toughness, *Acta Materialia* 286 (2025) 120727. <https://doi.org/10.1016/j.actamat.2025.120727>.
- [24] G. Plummer, B. Anasori, Y. Gogotsi, G.J. Tucker, Nanoindentation of monolayer $Ti_{n+1}C_nT_x$ MXenes via atomistic simulations: The role of composition and defects on strength, *Computational Materials Science* 157 (2019) 168–174. <https://doi.org/10.1016/j.commatsci.2018.10.033>.
- [25] Y.I. Jhon, Y.T. Byun, J.H. Lee, Y.M. Jhon, Robust mechanical tunability of 2D transition metal carbides via surface termination engineering: Molecular dynamics simulation, *Applied Surface Science* 532 (2020) 147380. <https://doi.org/10.1016/j.apsusc.2020.147380>.
- [26] C. Wei, C. Wu, Nonlinear fracture of two-dimensional transition metal carbides (MXenes), *Engineering Fracture Mechanics* 230 (2020) 106978. <https://doi.org/10.1016/j.engfractmech.2020.106978>.
- [27] H. Yu, K. Xu, Z. Zhang, X. Cao, J. Weng, J. Wu, Oxygen functionalization-induced crossover in the tensile properties of the thinnest 2D Ti_2C MXene, *J. Mater. Chem. C* 9 (2021) 2416–2425. <https://doi.org/10.1039/D0TC04637J>.
- [28] N. Nayir, Q. Mao, T. Wang, M. Kowalik, Y. Zhang, M. Wang, S. Dwivedi, G.-U. Jeong, Y.K. Shin, A. van Duin, Modeling and simulations for 2D materials: a ReaxFF perspective, *2D Mater.* 10 (2023) 032002. <https://doi.org/10.1088/2053-1583/acd7fd>.
- [29] Y. Chen, S. Tang, X. Yan, Manipulating the crack path through the surface functional groups of MXenes, *Nanoscale* 14 (2022) 14169–14177. <https://doi.org/10.1039/D2NR02235D>.
- [30] K. Ganeshan, Y.K. Shin, N.C. Osti, Y. Sun, K. Prenger, M. Naguib, M. Tyagi, E. Mamontov, D. Jiang, A.C.T. van Duin, Structure and Dynamics of Aqueous Electrolytes Confined in 2D- $TiO_2/Ti_3C_2T_2$ MXene Heterostructures, *ACS Appl. Mater. Interfaces* 12 (2020) 58378–58389. <https://doi.org/10.1021/acsami.0c17536>.
- [31] N.C. Osti, M. Naguib, A. Ostadhossein, Y. Xie, P.R.C. Kent, B. Dyatkin, G. Rother, W.T. Heller, A.C.T. van Duin, Y. Gogotsi, E. Mamontov, Effect of Metal Ion Intercalation on the Structure of MXene and Water Dynamics on its Internal Surfaces, *ACS Appl. Mater. Interfaces* 8 (2016) 8859–8863. <https://doi.org/10.1021/acsami.6b01490>.
- [32] L.F.V. Thomazini, A.F. Fonseca, Structure and elastic properties of titanium MXenes: Evaluation of COMB3, REAXFF and MEAM force fields, *Computational Materials Science* 259 (2025) 114134. <https://doi.org/10.1016/j.commatsci.2025.114134>.

- [33] Md.M. Billah, M.S. Rabbi, K.A. Rahman, P. Acar, Temperature and strain rate dependent tensile properties of titanium carbide/nitride MXenes, *Materials Chemistry and Physics* 312 (2024) 128581. <https://doi.org/10.1016/j.matchemphys.2023.128581>.
- [34] V.N. Borysiuk, V.N. Mochalin, Y. Gogotsi, Molecular dynamic study of the mechanical properties of two-dimensional titanium carbides Ti_n+1C_n (MXenes), *Nanotechnology* 26 (2015) 265705. <https://doi.org/10.1088/0957-4484/26/26/265705>.
- [35] Y. Li, C. Wei, S. Huang, C. Wu, V.N. Mochalin, *In-situ* SEM compression of accordion-like multilayer MXenes, *Extreme Mechanics Letters* 41 (2020) 101054. <https://doi.org/10.1016/j.eml.2020.101054>.
- [36] O. Lourie, D.M. Cox, H.D. Wagner, Buckling and Collapse of Embedded Carbon Nanotubes, *Phys. Rev. Lett.* 81 (1998) 1638–1641. <https://doi.org/10.1103/PhysRevLett.81.1638>.
- [37] S. Plimpton, Fast Parallel Algorithms for Short-Range Molecular Dynamics, *Journal of Computational Physics* 117 (1995) 1–19. <https://doi.org/10.1006/jcph.1995.1039>.
- [38] J.R. Gissinger, I. Nikiforov, Y. Afshar, B. Waters, M. Choi, D.S. Karls, A. Stukowski, W. Im, H. Heinz, A. Kohlmeyer, E.B. Tadmor, Type Label Framework for Bonded Force Fields in LAMMPS, *J. Phys. Chem. B* 128 (2024) 3282–3297. <https://doi.org/10.1021/acs.jpcb.3c08419>.
- [39] H.M. Aktulga, J.C. Fogarty, S.A. Pandit, A.Y. Grama, Parallel reactive molecular dynamics: Numerical methods and algorithmic techniques, *Parallel Computing* 38 (2012) 245–259. <https://doi.org/10.1016/j.parco.2011.08.005>.
- [40] A. Stukowski, Visualization and analysis of atomistic simulation data with OVITO—the Open Visualization Tool, *Modelling Simul. Mater. Sci. Eng.* 18 (2009) 015012. <https://doi.org/10.1088/0965-0393/18/1/015012>.
- [41] M. Khazaei, M. Arai, T. Sasaki, C.-Y. Chung, N.S. Venkataramanan, M. Estili, Y. Sakka, Y. Kawazoe, Novel Electronic and Magnetic Properties of Two-Dimensional Transition Metal Carbides and Nitrides, *Advanced Functional Materials* 23 (2013) 2185–2192. <https://doi.org/10.1002/adfm.201202502>.
- [42] W.C. Swope, H.C. Andersen, P.H. Berens, K.R. Wilson, A computer simulation method for the calculation of equilibrium constants for the formation of physical clusters of molecules: Application to small water clusters, *The Journal of Chemical Physics* 76 (1982) 637–649. <https://doi.org/10.1063/1.442716>.